AGU PUBLICATIONS

JGR

Journal of Geophysical Research: Solid Earth

RESEARCH ARTICLE

10.1002/2013JB010609

Key Points:
- New Zealand displays a wide variety of subduction slow slip behavior
- Some Hikurangi SSEs are associated with swarms of seismicity up to M4.8
- The Manawatu SSE has spatially offset tremor; most other SSEs have no tremor

Supporting Information:
- Readme
- Figure S1
- Figure S2
- Figure S3
- Text S1
- Text S2
- Text S3
- Animation S1
- Animation S2

Correspondence to:
N. M. Bartlow,
nbartlow@ucsd.edu

Citation:
Bartlow, N. M., L. M. Wallace, R. J. Beavan, S. Bannister, and P. Segall (2014), Time-dependent modeling of slow slip events and associated seismicity and tremor at the Hikurangi subduction zone, New Zealand, *J. Geophys. Res. Solid Earth*, *119*, 734–753, doi:10.1002/2013JB010609.

Received 16 AUG 2013
Accepted 30 DEC 2013
Accepted article online 4 JAN 2014
Published online 27 JAN 2014

Time-dependent modeling of slow slip events and associated seismicity and tremor at the Hikurangi subduction zone, New Zealand

Noel M. Bartlow[1,2], Laura M. Wallace[3], R. John Beavan[4,5], Stephen Bannister[4], and P. Segall[1]

[1]Department of Geophysics, Stanford University, Stanford, California,USA, [2]Now at Institute of Geophysics and Planetary Physics, Scripps Institution of Oceanography, University of California San Diego, La Jolla, California, USA, [3]Institute for Geophysics, University of Texas at Austin, Austin, Texas, USA, [4]GNS Science, Lower Hutt, New Zealand, [5]Deceased 19 November 2012

Abstract We present a time-dependent slip model of 12 slow slip events (SSEs) occurring in the Hikurangi margin of New Zealand during 2010 and 2011. This model is obtained by inverting daily GPS solutions from GeoNet's continuous GPS network on the North Island and northern South Island. We compare the properties of these SSEs to observations in Japan, Cascadia, and Mexico and find that Hikurangi SSEs have comparatively large amounts of slip (up to 27 cm), high slip rates (up to 1.4 cm/d), and a large range of depths (10–40 km), durations (7–270 days), and sizes (M_w 5.9–6.9). We further investigate the relationship between the Cape Turnagain SSE and an associated seismic swarm and find that observations are consistent with stress triggering outside the slowly slipping region; however, other explanations cannot be ruled out. We also compare slip during the long-term Manawatu SSE with the tremor epicenters found by Ide (2012) and note that tremor locations are offset in the downdip direction relative to the slipping region, similar to observations in the Bungo Channel of Japan and Guerrero, Mexico.

1. Introduction

In the last decade, slow slip events (SSEs) have been identified at many subduction margins worldwide that are well instrumented with continuous GPS. Although these events involve aseismic creep and are not dangerous by themselves, the hazard of large earthquakes on nearby portions on the plate interface may be increased during times of SSE slip [*Mazzotti and Adams*, 2004; *Segall and Bradley*, 2012]. Moreover, studies of SSEs and associated seismic phenomena provide important insights into the mechanics and physical conditions at subduction zone plate interfaces. In particular, SSEs in the Boso Peninsula area of Japan [*Ozawa et al.*, 2007a] and the Hikurangi subduction zone in New Zealand [*Wallace et al.*, 2012] have been shown to trigger seismicity with magnitudes in the *M*5 class. In Japan, there is evidence that the *M*9.0 Tohoku earthquake and/or its *M*7.3 foreshock were preceded by slow slip [*Kato et al.*,2011; *Ito et al.*, 2013]. It is therefore critical to study SSEs, and their relationships with triggered seismicity, in order to understand seismic hazard in subduction zones.

Slow slip events are inferred to occur on conditionally stable portions of the plate interface, in the transition from stick-slip (velocity weakening) behavior to aseismic creep (velocity strengthening) [*Dragert et al.*,2001; *Larson et al.*, 2004; *Ohta et al.*,2004, 2006; *Wallace and Beavan*, 2010]. Inferences from seismological, laboratory, and numerical modeling studies also suggest that slow slip and tremor occur in areas where pore fluid pressure is high and effective stress is low, on the order of 1–10 MPa [*Kodaira et al.*,2004; *Liu and Rice*, 2005, 2007; *Shelly et al.*, 2006; *Audet et al.*, 2009; *Song et al.*, 2009; *Bartlow et al.*, 2012; *Kitajima and Saffer*, 2012]. Whether or not these slow slip regions can also rupture seismically remains an open question, although evidence presented by *Ito et al.* [2013] suggests that large megathrust events may penetrate into SSE source regions. Tectonic tremor (composed of numerous low-frequency earthquakes [e.g., *Shelly et al.*, 2007]) often accompanies slow slip and is thought to be a type of slip on the plate interface [*Ide et al.*, 2007; *Brown et al.*, 2009]. In Nankai and Cascadia, SSEs are accompanied by abundant tectonic tremor that is concurrent and colocated with migrating geodetically resolved slow slip [*Hirose and Obara*, 2010; *Bartlow et al.*, 2011]. However, in other areas, such as the Bungo Channel in Japan or the Guerrero seismic gap in Mexico, tremor is offset downdip from the slipping region [*Hirose et al.*, 2010; *Kostoglodov et al.*, 2010]. Since the relationships between slow slip and tremor can vary by location, it is important to study SSEs in as many regions as possible to sample the full range of behaviors.

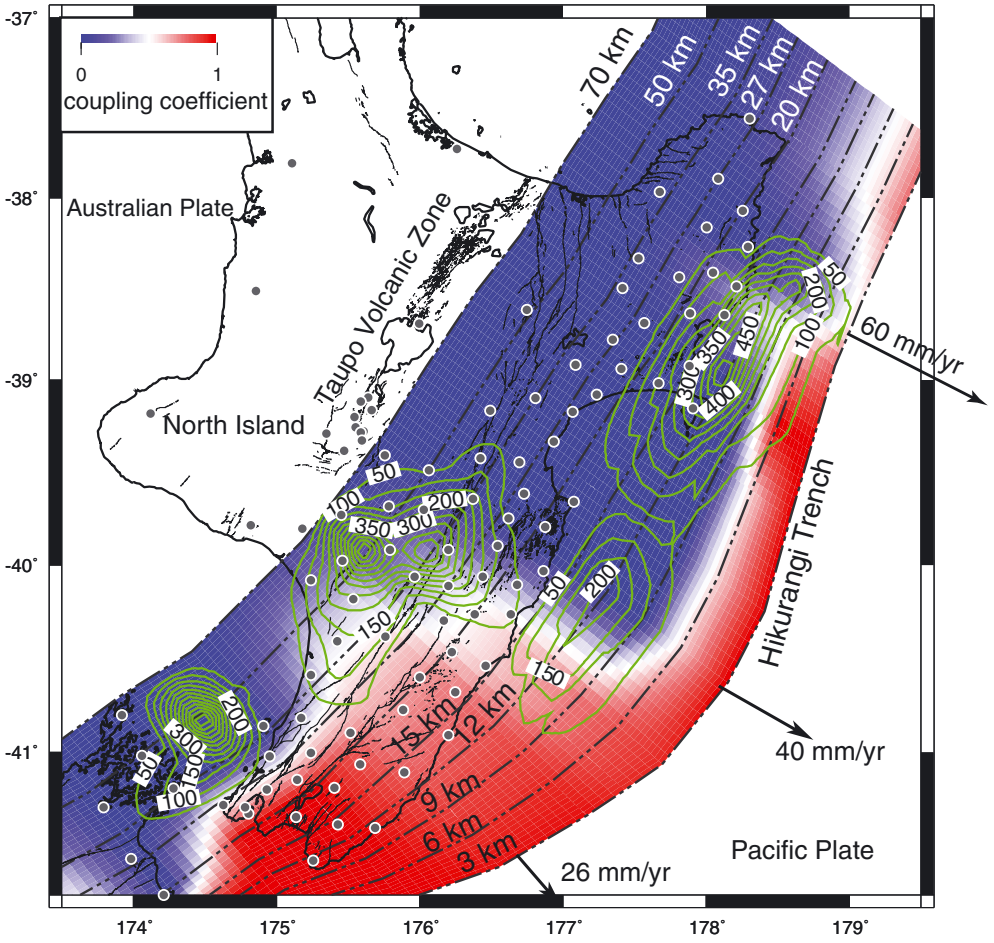

Figure 1. Locations of GPS stations used in this study. Color shows plate locking averaged through SSEs. Green contours show locations of known slow slip events identified between 2002 and 2010. This figure is adapted from *Wallace and Beavan* [2010].

In this study, we use the Network Inversion Filter (NIF) [*Segall and Matthews*,1997; *McGuire and Segall*, 2003; *Miyazaki et al.*,2006] to examine a complex sequence of SSEs during the late 2009 to early 2012 period in the Hikurangi subduction zone of New Zealand [*Wallace et al.*, 2012] using daily GPS solutions from the GeoNet network (www.geonet.org.nz). The Hikurangi subduction zone is known to have a diverse array of SSEs, with a large range of durations, depths, sizes, and recurrence intervals [*Wallace and Beavan*, 2010]. The 2010–2011 sequence is especially well suited to analysis by the NIF because there are many SSEs, some of which migrate and some of which overlap in time with other SSEs. The NIF provides a method for performing a single inversion of time series data to obtain a time-dependent model of the behavior of every SSE and is not hindered by SSEs overlapping in time even if the signals potentially interfere at some stations. We compare our time-dependent slip model with tremor and seismicity to study their relationships and compare these observations to the relationship between slip, tremor, and microseismicity in other subduction zones. This study builds on the work of *Wallace et al.* [2012], which also studied this sequence of events, but represents an advance in the modeling technique used and a slight extension of the time period considered. In particular, using the NIF allows us to study migrations of slip during SSEs in more detail and to identify previously unknown smaller SSEs in this time period.

2. Tectonics and Slow Slip in the Hikurangi Subduction Zone

The Hikurangi subduction margin accommodates westward subduction of the Pacific Plate at the Hikurangi trough at rates that increase from 2.5 cm/yr in the south to more than 6 cm/yr at the northern Hikurangi margin (Figure 1). The threefold northward increase in convergence rate occurs due to rapid clockwise rotation of the forearc (at 3–4°/Myr) about nearby poles of rotation, relative to the Australian and Pacific Plates [*Wallace et al.*, 2004]. In the region of the Hikurangi Trough, the Pacific Plate is composed of the Hikurangi

Plateau, a Cretaceous Large Igneous Province [*Mortimer and Parkinson*, 1996]. Subduction of the plateau has caused much of the forearc to become subaerial and provides an excellent setting to use land-based techniques to study processes occurring on the shallow subduction thrust. The subducting slab and subduction interface geometry is revealed by seismicity [*Ansell and Bannister*, 1996], seismic tomography [*Eberhart-Phillips et al.*, 2005; *Reyners et al.*, 2006], and active source seismic studies of the offshore portion of the margin [*Barker et al.*, 2009].

GPS studies have revealed that the southern Hikurangi subduction interface is strongly coupled to 30–40 km depth, while the northern Hikurangi margin is dominated by aseismic creep [*Wallace et al.*, 2004, Figure 1]. Slow slip events have been observed on the Hikurangi subduction thrust since 2002 with the development of a continuous GPS network in the North Island as part of the New Zealand Earthquake Commission-funded GeoNet project [*Douglas et al.*, 2005; *Wallace and Beavan*, 2010]. Slow slip events appear to occur along the downdip limit of interseismic coupling, including some events that follow the along-strike transition from shallow to deep coupling (Figure 1). There are marked along-strike variations in slow slip event characteristics at the Hikurangi margin. Deep Hikurangi slow slip events occur at 25–60 km depth, recur every 2–6 years, last 2 months to 1 year, and involve an equivalent moments in the range of M_w6.5–7.0 [*Wallace and Beavan*, 2006; *Wallace and Beavan*, 2010; *Wallace and Eberhart-Phillips*, 2013]. These SSEs occur mainly in the southern part of the Hikurangi margin, where plate locking extends deeper (Figure 1). Shallow Hikurangi SSEs occur at less than 15 km depth, typically last 1–3 weeks, recur every 1–2 years, and span a range of equivalent moments from M_w 6.5 to 6.8 based on previous studies [*Wallace and Beavan*, 2010; *Wallace et al.*,2012]. These shallow SSEs occur mainly in the northern part of Hikurangi, where plate locking is confined to the shallowest part of the interface (Figure 1). In the central part of the Hikurangi margin, both deep and shallow SSEs occur with a gap in between [*Wallace and Eberhart-Phillips*, 2013].

These along-strike variations in coupling and slow slip are accompanied by along-strike variations in subduction margin characteristics, including: a dramatic southward increase in sediment thickness on the incoming plate, a shift from a well-developed accretionary wedge in the south, to a margin dominated by frontal subduction erosion (and seamount subduction) in the north, and a shift from back-arc extension in the north to upper plate transpression in the south (see review in *Wallace et al.*, 2009). The physical controls on along-strike variations in interseismic coupling and slow slip at Hikurangi are currently unknown, although some studies suggest that upper plate bedrock structure [*Reyners and Eberhart-Phillips*, 2009] and the state of stress in the upper plate may be key factors influencing this coupling variation [*Fagereng and Ellis*, 2009]; however, debate continues and the results of *Townend et al.* [2012] partially contradict earlier studies. It is also likely that along-strike variations in roughness of the incoming plate [e.g., *Wang and Bilek*, 2011], strong spatial variations of interface frictional properties, and the presence of fluid overpressures have a major influence on the diverse slip behavior of the Hikurangi subduction interface [*Bell et al.*, 2010; *Wallace et al.*, 2012].

Although previous studies have observed some triggered and ambient tremor close to the locations of New Zealand SSEs [*Fry et al.*, 2011; *Kim et al.*, 2011; *Ide*,2012], the relationship between slow slip and tremor there is not clear, nor are observations of tremor ubiquitous. This study elaborates further on the relationship between observed tremor locations and the location of slip during the long-term 2010–2011 Manawatu SSE (see section 7). We also contrast the SSEs and associated seismicity at Hikurangi with the well-known Cascadia and Nankai episodic tremor and slip (ETS) to give important insights into the physical mechanisms behind SSE and ETS occurrence (see section 8). Similar to SSEs at Boso Peninsula, central Japan [e.g., *Sagiya*, 2004; *Ozawa et al.*,2007a], previous studies have shown that central and north Hikurangi SSEs are characterized by elevated levels of microseismicity (relative to normal background rates) [*Delahaye et al.*, 2009; *Wallace et al.*,2012]. In this study, we further investigate the details of the possible triggering relationship between the 2011 Cape Turnagain SSE and a swarm of earthquakes that accompanies it (see section 6.1).

3. Data and Methods

In this study we invert daily GPS solutions from a network of continuous GPS (cGPS) stations on the North Island and northern South Island of New Zealand. The cGPS and seismic network in New Zealand is installed and operated by the New Zealand GeoNet project (Figure 1). Further information on the network and the basic data are available at www.geonet.org.nz. GPS data processing methods are outlined on the GeoNet website and described more fully in *Wallace and Beavan* [2010]. The cGPS data is analyzed

by GeoNet using Bernese v5.0 [*Dach et al.*, 2007] software holding IGS08 orbits and Earth orientation parameters fixed (see *Wallace et al.* 2012 for more details). The resulting daily-coordinate time series are regionally filtered [*Wdowinski*, 1997; *Beavan*,2005] using a set of NZ stations that have close to linear behavior over the 2002–2011 time period. Regionally filtered time series for each site are available at www.geonet.org.nz/resources/gps/timeseries.

Before inverting the daily cGPS position time series, we remove secular velocities and seasonal signals. For seasonal signals, we solve for the amplitudes and phases of sinusoidal signals having 12 and 6 month periods at each component of each station. The secular velocities we wish to remove are the velocities of the stations during the inter-SSE period, while no plate interface slip is occurring. Therefore, we use a Kalman filter to fit secular velocities and seasonal signals to the time series data only during inter-SSE periods, and allow for offsets during data gaps and SSE periods. The specific Kalman filter approach is described in *Bartlow et al.* [2011] and *Miyazaki et al.* [2006]. The regionally filtered time series with secular and seasonal terms removed are then used for the time-dependent inversion. Seasonal signals are generally small in Hikurangi; examples of the fits of seasonal signals to selected time series can be seen in Figures S1 and S2 in the supporting information.

To perform a time-dependent inversion of the cGPS positions for slip and slip rate on the plate interface, we use the Network Inversion Filter (NIF) [*Segall and Matthews*,1997; *Miyazaki et al.*,2006; *Bartlow et al.*, 2011]. We use a triangular mesh of the interface as specified in *Ansell and Bannister* [1996], with the shortest sides of each triangle being about 12 km. Elastic half-space Green's functions are calculated for each triangle assuming a Poisson's ratio of 0.25 following *Thomas* [1993], with slip direction specified for each triangle using the tectonic block model of *Wallace et al.* [2004]. While varying the slip direction may provide a slightly better fit to the data, it almost doubles the number of free parameters to be fit by the model. *Wallace and Beavan* [2010] showed that inverting for the rake of the slow slip patches gives slip vector directions consistent with those predicted by the block model of *Wallace et al.* [2004].

The NIF solves for time-dependent slip and slip rate on each element of a specified plate interface mesh using Kalman filter approach. The forward model for the GPS position time series is the following:

$$X(t) = X(0) + \boldsymbol{G}s(t) + \boldsymbol{F}f(t) + L(t) + \epsilon \tag{1}$$

where $X(t)$ is a vector containing all GPS stations positions at time t, $X(0)$ is a vector of initial positions, $\boldsymbol{G}$ is a matrix of elastic Green's functions mapping slip to GPS displacement, $s(t)$ is a vector containing slip on each fault element at time t, $\boldsymbol{F}$ is a matrix representing a whole network translation, $f(t)$ is the time-dependent scalar reference frame wobble noise term, $L(t)$ is a vector containing the amplitude of random walk noise for each station at time t, and ϵ represents white noise. The NIF steps through the data 1 day at a time and keeps track of slip (s) and slip rate ($\dot{s}$) for each triangular subfault at each time step. The NIF first performs a prediction step in which the slip at the new time step is calculated, based on the current estimate of slip rate, as $s(t+1) = s(t) + \dot{s}(t)\Delta t$. Uncertainty on both slip and slip rate increase during the prediction step. The NIF then updates this prediction with data, as the optimal linear combination of information from past states (prediction step) and the current measurements (update step). After the NIF steps forward through the data, it performs a "smoothing" process stepping backward through the data. This backward smoothing results in the model being dependent on all data at all time steps, rather than just past data, and is more stable to small changes in data.

The NIF includes both spatial and temporal smoothing parameters (γ and α, respectively), implemented following *Miyazaki et al.* [2006]. The temporal smoothing parameter α, together with the data uncertainties, control the relative weighting of the prediction and update steps of the NIF. Spatial smoothing γ is a relative weighting between fitting the data as in equation (1) and minimizing some functional of the model, often the discrete Laplacian as in this study. Because of temporal smoothing, NIF outputs can be acausal with slip appearing in the model a few days before measurable offsets are seen in the GPS data. Tradeoffs exist between γ and the spatial extent of the SSEs, and α and the duration of the SSEs. The choice of spatial and temporal smoothing parameters is an important part of the NIF, although factors of 2–3 in either parameter do not affect the model significantly. While variations on the NIF can use temporally or spatially variable smoothing parameters [*Fukuda et al.*, 2004], for simplicity, we choose a single value of spatial and temporal smoothing for this model.

Often, these smoothing parameters are selected by a maximum likelihood estimation (MLE) method [see *Segall and Matthews*, 1997], which chooses the hyperparameters α and γ under which the observed data is most likely. This optimization is usually done by grid search of α and γ space, since local maxima may exist. In this case, the large amount of data made a grid search too computationally intensive. We ran the MLE grid search on smaller subsets of data at times of particular SSEs but discovered that the MLE method gave us very different values for the different time periods. This is probably due to the large variation in slip rates, patch sizes, and durations of SSEs in the Hikurangi subduction zone (see section 5). Additionally, the maximum in the likelihood function is broad, with a wide range of models with high likelihood. Therefore, the final values of the smoothing parameters ($\alpha = 50$ and $\gamma = 0.025$) were chosen by visual inspection of the model and data fits. These values are very similar to the values used in *Bartlow et al.* [2011] for inversion of the August 2009 central Cascadia ETS event.

For reasons that are poorly understood, some of the cGPS stations in New Zealand are particularly prone to large outliers in position time series data. Therefore, we employed a simple outlier removal method on the GPS time series. Using a sliding window of six data points, we calculated a mean position and identified as outliers any data in the window whose 3-D position is more than 4 mm away from the mean. Each data point appears in six windows and is marked as an outlier if it tests positive in any window. Examples of data before and after outlier removal are shown in Figure S3. The GPS position time series noise is modeled in the NIF as white noise with variance $(3\ \text{mm})^2$ in the horizontal position and $(6\ \text{mm})^2$ in the vertical position, and random walk noise with amplitude $1\ \text{mm}/\sqrt{\text{year}}$. White noise variance levels were chosen by inspecting histograms of data with outliers removed, corrected for inter-ETS velocities and seasonal signals, from multiple stations during quiet periods. Random walk amplitude was chosen by inspecting power spectra of data from multiple stations also during quiet periods.

For this study we also use catalogs of seismicity and tremor for comparison to the geodetically inferred slip model. The main seismicity catalog we use is from GeoNet and includes earthquakes at depths up to 100 km over the entire study area (http://magma.geonet.org.nz/resources/quakesearch/). Earthquakes are located using a standard one-dimensional velocity model for New Zealand, except in the Taupo and Wellington areas where different one-dimensional velocity models are used. More details about the hypocenter location and magnitude determination can be found at http://info.geonet.org.nz/display/appdata/Hypocentre+Derivation.

The GeoNet catalog is complete to $\sim M$ 2.5. The largest earthquake in the catalog during the period analyzed here is a magnitude 5.7 event, perhaps just large enough to cause small displacements at a few GPS stations, and smaller than the magnitude of our smallest detected SSE. As earthquakes are a relatively insignificant source of deformation compared to SSEs during this time period, we do not correct for earthquake offsets in the GPS data. GeoNet also maintains a catalog of earthquake moment tensors, from which focal mechanisms can be derived. We have reproduced the relevant moment tensors from this catalog as Table S1. In section 6 we discuss one of these focal mechanisms. The tremor catalog we use is from *Ide* [2012], with methods outlined in that publication. It covers the time period of late 2004 until early 2010.

For the 2011 Cape Turnagain swarm (see section 6), we are interested in the precise locations of earthquakes in the swarm. The depths of these earthquakes are especially important to their physical interpretation, as the earthquakes could be within the subducting slab, on the plate interface, or within the accretionary wedge. To explore how well constrained the depths of these earthquakes are, we relocate the relevant subset of the GeoNet seismic catalog. First, we relocate the earthquakes using the New Zealand wide 3-D velocity model of *Eberhart-Phillips et al.* [2010] using manually picked *P* and *S* phase times, supplementing original picks carried out by GeoNet. Then we refine these locations using the double-difference (DD) tomography algorithm of *Zhang and Thurber* [2003], which builds on the DD location procedure of *Waldhauser and Ellsworth* utilizing differential times of *P* and *S* phase times. Google Earth .kml files of both sets of locations are included in the supporting information as kml files S1 and S2. The technique minimizes residuals between observed and calculated arrival-time differences for pairs of closely located earthquakes, while also minimizing the residuals of absolute arrival times. These derived differential times were weighted based on the quality of the arrival time measurements. Velocities are held fixed, again using the model of *Eberhart-Phillips et al.* [2010].

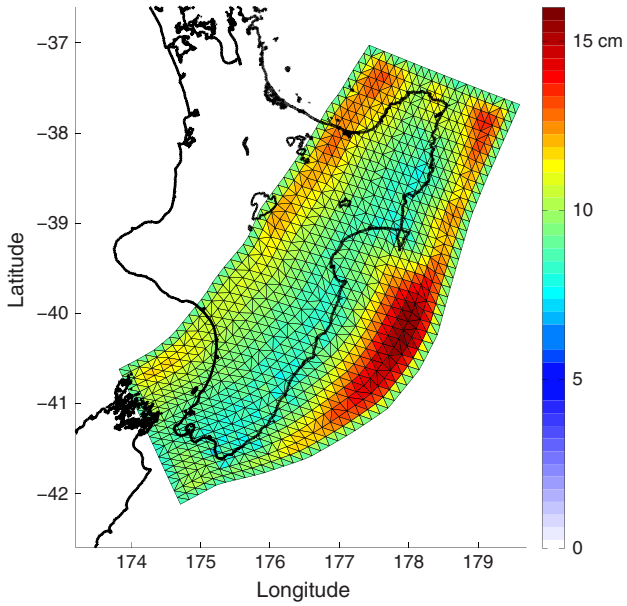

Figure 2. Formal error on the total slip produced by the NIF (diagonal elements of the slip covariance matrix). The uncertainty increases with the time period considered; this plot shows the uncertainty over the 2 year time period are shown. Smaller time intervals yield smaller uncertainties with the same spatial pattern.

4. Model Resolution

The NIF estimates a covariance matrix for the slip and slip rate at each time step. The diagonal of the covariance of the slip at the final time step gives an estimate of the formal error in the total slip for the entire time period (Figure 2). This map shows that slip is not as well-resolved offshore or on the deeper extent of the plate interface. The poor offshore resolution is a result of the lack of stations, and the poor resolution on the western edge of the model is due to the increasing plate interface depth. Slip is constrained to taper to zero just outside the mesh, so the formal error also tapers down at the edge of the mesh as well. The choice to taper slip to zero at the shallow limit of the model is arbitrary and alternatives, such as tapering the spatial derivative of slip to zero, would be equally valid and potentially include more slip in the shallow region.

A checkerboard test of the model resolution using 50 km by 50 km squares is shown in Figure 3. Synthetic GPS data was calculated at the locations of all 113 stations used in this study, with added white noise with 3 mm standard deviation in the horizontal and 6 mm standard deviation in the vertical. This synthetic data was inverted using the NIF with all smoothing and noise parameters equal to those used in the inversion

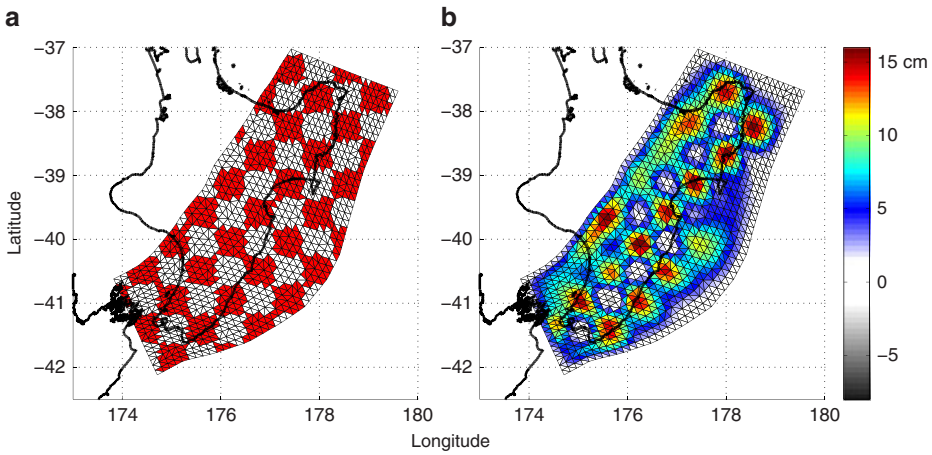

Figure 3. Single checkerboard test for model resolution. Checkers are 50 km in size. (a) Specified forward slip model with 14 cm of slip in the checkers and (b) NIF result from inverting noisy synthetic GPS data (see text).

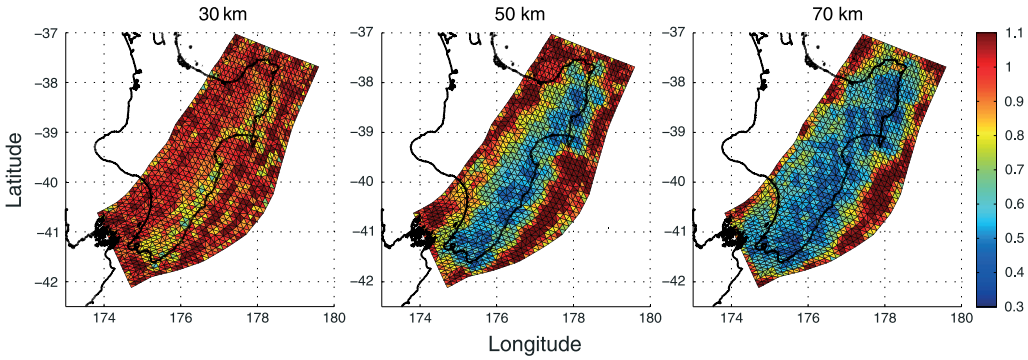

Figure 4. Average error from multiple checkerboard tests. Each figure shows a nondimensional average error (see text for definition) from multiple checkerboard tests with checkers of the indicated size and 14 cm of slip.

of the actual data. The time-dependent slip model is defined as follows: for the first 5 days, no slip occurs and the synthetic data is just the white noise; for the next 20 days, the slip ramps up linearly to 14 cm in the checkerboard pattern shown in Figure 3a; and for the final 5 days, slip remains constant at 14 cm and no further slip occurs. The final slip model obtained by the NIF is shown in Figure 3b. This serves to give an idea of where the data can resolve 50 km patches and the effect of spatial smoothing.

Clearly, larger patches of slip will be better resolved than smaller patches for the same slip amplitude. The formal model error indicates the variance of the slip for each triangle but does not indicate whether the data can resolve slip on these spatial scales. Checkerboard tests are useful for illustrating spatial resolution, but a single checkerboard test does not give a complete picture because the results depend on the specific locations of the checkers. Therefore, we choose three checkerboard patch sizes (30, 50, and 70 km), and for each size, we run 25 checkerboard tests with the checkers in different locations. We also allow the patch sizes to vary randomly within 10% of the specified size. For each checkerboard test, we compute an error vector as follows:

$$\text{error} = \text{abs}(\text{slip}_{\text{NIF}} - \text{slip}_{\text{checker}})/7 \text{ cm} \quad (2)$$

where slip_{NIF} is the NIF model of slip and $\text{slip}_{\text{checker}}$ is the input forward model. We divide by 7 cm because it represents a spatially averaged slip value and also represents the error produced by a spatially uniform model with the same total moment. We average the computer error vectors over the 25 models for each of the three patch sizes. The results of this test are shown in Figure 4. An error value close to 1 indicates little to no resolution, while values less than 0.5 indicate reasonably well-resolved areas. Well-resolved areas have error values significantly higher than zero because spatial smoothing causes checkers to be smeared out, with slip higher than the forward model in the center of a slip patch, and slip lower than the forward model near the edge of a slip patch.

This test shows that 30 km patches are not resolved by the data anywhere. Instead slip estimated by the NIF gets smeared out in an almost uniform distribution (Figure 4a). Fifty kilometer patches have good resolution in the central model region but are unresolved offshore and on the deepest extent of the plate interface (Figures 3 and 4b). Seventy kilometer patches are well resolved in most of the model region (Figure 4c), except the far offshore area and some of the deepest extent of the interface. All panels of Figure 4 show a similar spatial pattern to the formal error in slip seen in Figure 2. Comparison of Figures 3 and 4b shows how the value of the error function defined in equation (2) relates to checkerboard tests of resolution.

While this test is preferable to a single checkerboard test, it does have limitations. The lack of resolution offshore may be overestimated when applied to realistic slip distributions, because in a checkerboard pattern, the larger signals generated by slip patches onshore near stations interfere with the detection of the smaller signals created by offshore slip patches. In reality, transient offshore slip almost always occurs without simultaneous onshore slip and may therefore be better resolved. This analysis also does not address how resolution changes with the choice of smoothing parameters, or the potential biases introduced by inaccurate elastic Green's functions, an inaccurate fault plane model, or inaccurate modeling of seasonal signals or common mode errors.

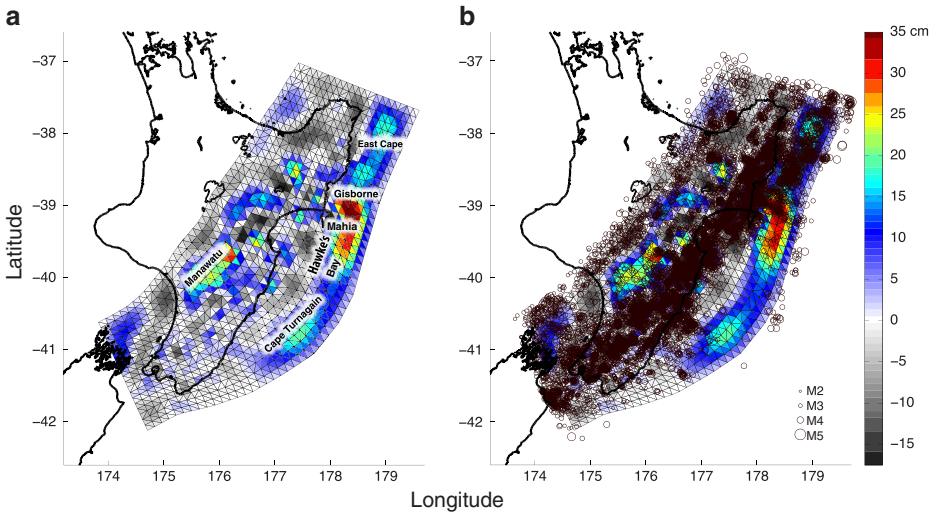

Figure 5. (a) Cumulative transient slip for the 2 year period 14 December 2009 to 13 December 2011. (b) Same as Figure 5a, with the addition of seismicity with magnitude greater than 2.5 during the same period within ±10 km of the plate interface where the plate interface depth is 20 km or deeper, and all seismicity with depths of 35 km or shallower in the region where the plate interface is shallower than 20 km.

5. Results From the Full Time-Dependent Inversion

Animation S1 shows the slip rate on the plate interface as a function of time, along with GPS displacements (vectors). The total slip is plotted in Figure 5. Whether or not the slow slip patches in the offshore Hawke's Bay and offshore Cape Turnagain areas are connected, as shown in Figure 5a, or there really is a gap without slow slip between them, is not resolved. Models both with or without slip on the interface east of Hawke's Bay can adequately fit the data, and small changes in spatial and temporal smoothing parameters change whether or not these slow slip patches appear connected. Our model also does not resolve whether or not the shallow SSEs rupture all the way to the seafloor at the Hikurangi trench, or, alternatively, if there is a region without slow slip updip of these slow slip patches. Because slip is tapered to zero at the edge of the model, we show no slip at the trench; however, there may in fact be unresolved slip in this region.

Using the results of the NIF as a guide for when and where SSEs occurred, we visually inspect data to confirm slow slip events and to obtain starting and ending dates of individual SSEs. Visual inspection is especially important for smaller SSEs, as some are close to the level of model noise. We identify 12 separate SSEs (see Table 1). For each SSE, we also calculate a maximum stress drop. To do this, we calculate the stress at the centroid of each triangle caused by cumulative slip on all other triangles using Hooke's law, assuming a shear modulus of 30 GPa and a Poisson's ratio of 0.25. Stress drops are calculated as the difference between stress 3 days after the end of the SSE and stress 3 days before the onset of SSE slip as given in Table 1.

Slow slip events in this model show wide ranges of total slip (1.2–27 cm), peak slip rate (0.23–1.4 cm/day), duration (7–270 days), moment magnitude (M_w) (5.8–6.9), depth (10–40 km), and peak stress drop (20–390 kPa). Therefore, there is no "typical" Hikurangi SSE, rather this subduction zone displays a wide range of SSE behavior. The total cumulative moment over the entire 2 year period is 1.25×10^{20} Nm, equivalent to a moment magnitude of 7.4. Although the magnitude of SSE slip generally increases with duration, there is much scatter and the duration of an SSE in Hikurangi does not determine its magnitude (Figure 6a). This is in contrast to observations in Cascadia, which show a much stronger relationship between duration and magnitude [*Aguiar et al.*, 2009]. The appears to be no correlation, or at most a weak correlation, between magnitude and stress drop (Figure 6b), consistent with the lack of scaling between magnitude and stress drop observed for regular earthquakes, although these stress drops are calculated differently [e.g., *Shaw*, 2009; *Baltay et al.*, 2011]. A correlation is observed between duration and stress drop (Figure 6c), with longer duration events having higher stress drops. A least squares regression yields a best fitting power law of stress drop = 9 duration$^{.66}$.

In Table 1, we list only SSEs that are visible in the GPS data at a minimum of two stations. However, in the East Cape region, where the smallest identified SSEs occur, there are many small transients that show

Table 1. Summary Table of SSEs Observed in the Hikurangi Subduction Zone, Late 2009 to Early 2012[a]

Name	Starting Year	Starting Day	Duration (days)	Slip Rate, (cm/d)	Total Slip (cm)	M_w	Depth, (km)	Stress Drop (kPa)
East Cape, Mahia, and Hawke's Bay 1	2010	24	36	0.51	7.3	6.8	10	110
Gisborne 1	2010	74	27	1.4	21	6.9	10	180
Manawatu	2010	159	270	0.60	27	6.9	40	390
East Cape 2	2010	195	7	0.23	1.2	6.2	20	20
Gisborne 2	2011	53	9	0.28	2.4	6.4	10	40
East Cape 3	2011	112	18	0.23	3.2	6.2	20	40
Cape Turnagain	2011	171	30	0.70	7.4	6.6	10	60
Mahia 2	2011	184	7	0.33	3.1	6.1	20	70
Hawke's Bay 3	2011	223	15	0.48	4.1	6.5	20	50
East Cape 4	2011	254	28	0.27	6.0	6.3	10	60
Mahia 3	2011	304	14	0.26	2.6	5.9	20	50
Gisborne 3	2011	341	21	0.67	5.8	6.5	10	70

[a]Starting dates and durations are approximate. Slip rates represent peak values during each SSE. Depth is reported for the area of maximum slip to the nearest 10 km. Stress drops are calculated assuming a 30 GPa shear modulus and Poisson's ratio of 0.25. Stress drops are peak values for each SSE and are reported to the nearest 10 kPa.

up only on station PUKE. These can be clearly seen in the PUKE time series, which is available online (see section 3). These transients may be signatures of even smaller SSEs, but we cannot confirm them as real SSEs due to lack of station coverage. Since these signals show up only on PUKE, it is possible that these transients are occurring on other crustal faults or could be due to another source entirely.

The SSEs and seismicity have a mostly complementary spatial pattern (Figure 5b). Patches of the plate interface with SSEs appear to have little to no seismicity. In Figure 5b, we plot all earthquakes within ± 10 km of the plate interface. In fact, most of the plotted earthquakes are likely not on the interface although some are. In particular, the strong band of seismicity updip from the Manawatu patch is known to occur in two regions of high seismic activity, one above the interface and one below the interface, with a lack of seismicity actually on the interface [*Reyners and Eberhart-Phillips*, 2009]. The complementary distribution of SSEs and microseismicity suggest that the subduction zone frictional properties are heterogeneous, with discrete patches that tend to rupture aseismically in slow slip, while the physical properties of other portions of the interface promote faster rupture that generates seismic waves [*Reyners and Eberhart-Phillips*, 2009]. This is also supported by the plate locking model of *Wallace and Beavan* [2010] which uses campaign GPS measurements to show little to no long-term plate locking (e.g., slip deficit) in the slow slip regions (Figure 1). Additionally, an inversion for plate locking during the inter-SSE period shows near full locking in the SSE regions between slow slip events, implying that most or all of the plate motion is accommodated by slow slip in these regions, at least during the last 15–20 years [*Wallace and Beavan*, 2010].

The earthquake catalog (plotted in Figure 5b) contains seismic swarms that are possibly associated with SSEs in the Cape Turnagain and Gisborne regions. The Cape Turnagain swarm was reported in *Wallace et al.* [2012], who observed that the earthquakes migrate northward, as does the slip. We investigate the relationship between slip and seismicity for this swarm further in section 6. The Gisborne area is more complex because it has multiple SSEs, more swarms, and swarms not associated with SSEs. This makes a

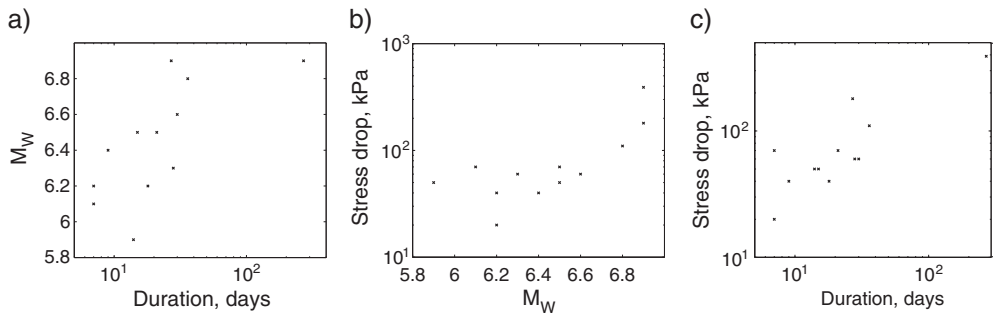

Figure 6. (a) Duration-magnitude plot, (b) plot of magnitude versus stress drop, and (c) plot of duration versus stress drop for all SSEs in Table 1. Note durations and stress drops are plotted on log scales.

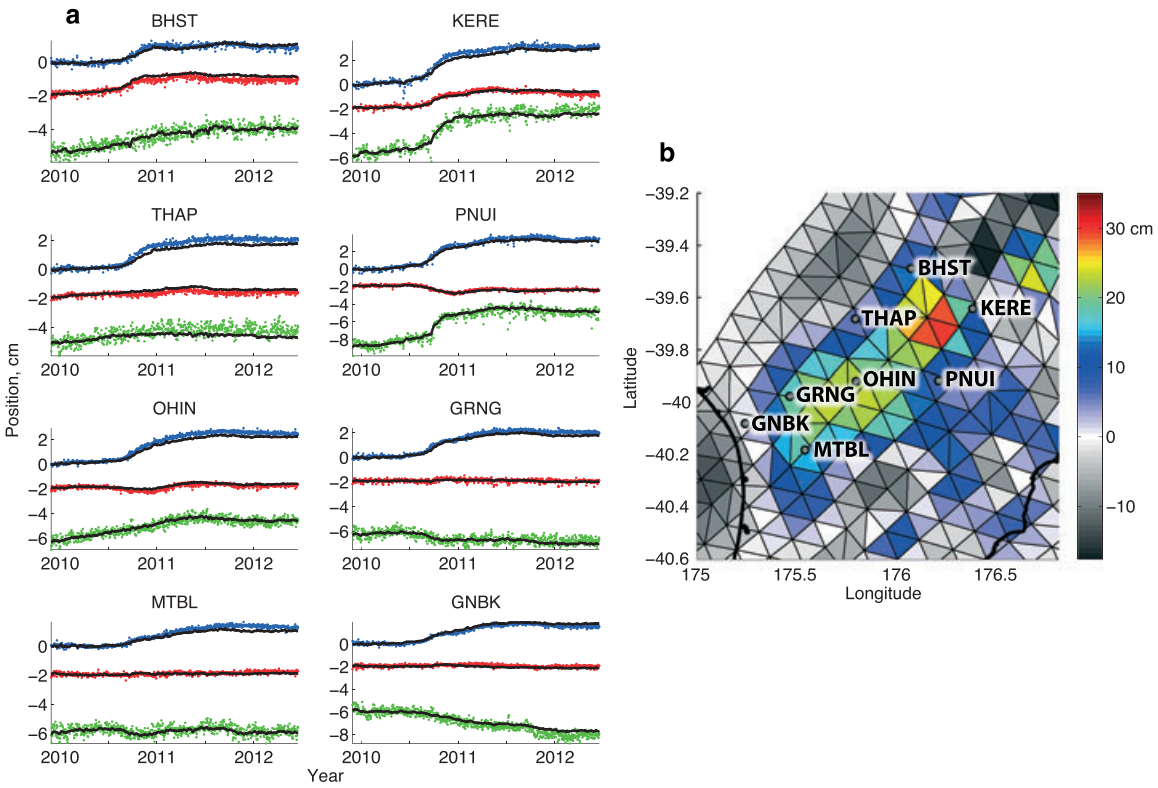

Figure 7. (a) Time-dependent fit to data for selected stations in the Manawatu area. Colored dots are data with outliers, seasonal signals, and inter-ETS velocities removed. Reference frame wobble as fit by the NIF is also removed. Black lines are model fits. Stations are ordered north to south. (b) Map of stations in Figure 7a, with final slip distribution.

demonstrating a causal link between SSEs and seismic swarms more difficult in the Gisborne region. In this study, we do not investigate these swarms in detail.

5.1. The 2010–2011 Manawatu SSE

Time-dependent data fits for the 2010–2011 Manawatu SSE are shown in Figure 7. In general, the model fits the data well; however, at a few stations (e.g., THAP and KERE), the model slightly underpredicts the east component of displacement (Figure 7). This could be due to inaccurate physical assumptions in the model, such as homogenous halfspace Green's functions, an inaccurate plate interface location, or an inaccurate specified slip direction. In general, the total slip estimated for this SSE matches well with previous slip models from static GPS inversions of *Wallace et al.* [2012].

The Manawatu SSE occurs in three stages. Stage 1 is characterized by a brief episode of slip, lasting approximately 1 week, as seen in Figure 8a. After a brief quiescence, stage 2 begins. This stage is the largest and longest, lasting for approximately 5 months, as seen in Figures 8d–8g. There is a period of reduced slip rate before the third stage (Figure 8h). The third stage occurs further south than the first two stages and lasts approximately 3.5 months (Figures 8i–8l). This multipulse pattern can be seen in the data by eye at some stations, for example, PNUI, GRNG, and GNBK (Figure 7a). This shows that Manawatu SSEs are not simple events with single acceleration and deceleration phases, but rather accelerate and decelerate multiple times in a single SSE.

5.2. The 2010–2011 East Coast SSE Sequence

At east coast stations, the model is able to fit the data well (Figure 9). At some stations (e.g., AKTO and PUKE) the model prediction exhibits high-frequency fluctuations that presumably reflect noise in the data. This high-frequency component could be removed by changing the temporal smoothing parameter. However, temporally smoother models are unable to fit the rapid SSE deformation seen at stations in the Gisborne area (e.g., MAHI and CNST). The Monte Carlo mixture Kalman filter (MCMKF) of by *Fukuda et al.* [2004] is meant to address this type of problem; however, it is extremely computationally intensive. We do not attempt this method in this study.

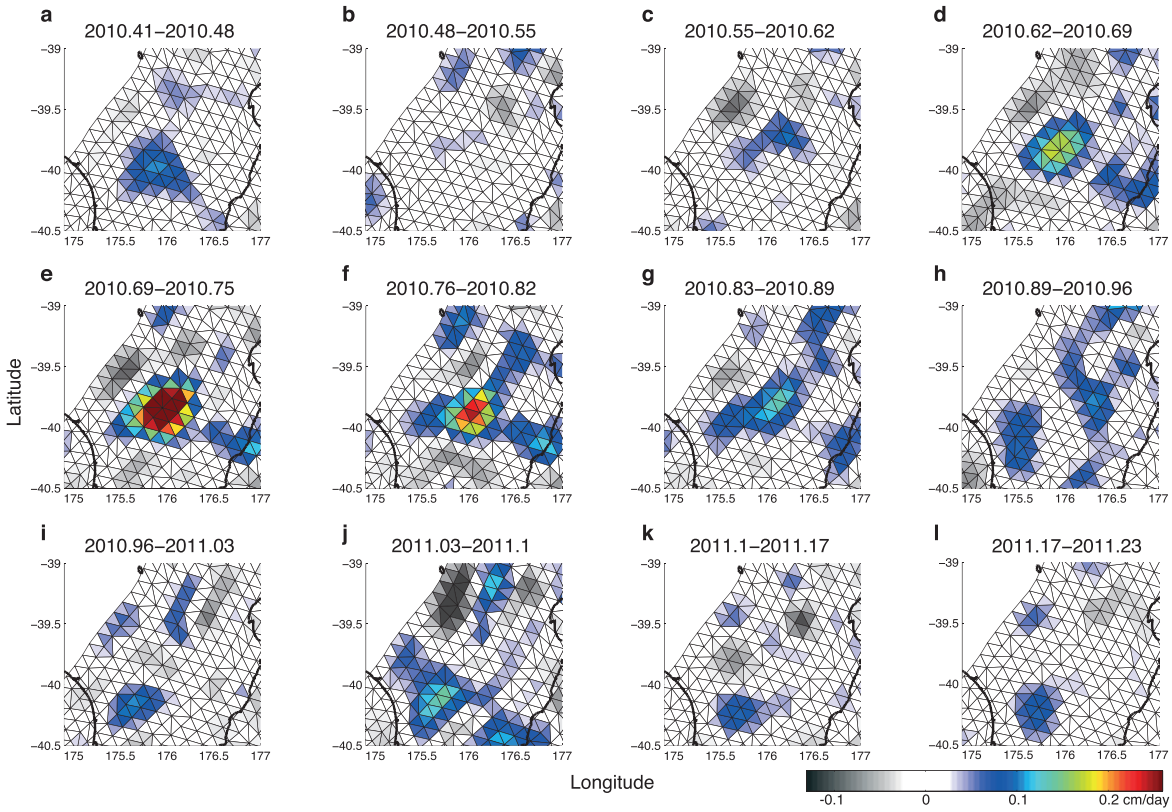

Figure 8. (a) Snapshots of slip rate for the Manawatu SSE, averaged over 16 day intervals. Two phases are clearly seen; the first phase ends around decimal year 2010.9, with a second, weaker phase beginning further to the south around decimal year 2010.95.

Together, the Gisborne, Hawke's Bay, East Cape, and Cape Turnagain events constitute the 2010–2011 East Coast SSE sequence. Similar to previous results, we see multiple slow slip events with periods of quiescence in between [*Wallace et al.*, 2012]. The events do not occur in a simple south-to-north or north-to-south order, instead jumping around on the plate interface. As reported in *Wallace and Beavan* [2010], we observe simultaneous slow slip in February 2010 on the East Cape and Hawke's Bay patches, with the Gisborne region not slipping in between (see Table 1). The central region then has a large slow slip event beginning in March 2010. Stress changes from the earlier SSE in the region of the March 2010 Gisborne SSE calculated from our slip model are 70–100 kPa, pointing to a likely triggering relationship between SSE patches in the Gisborne area. A similar pattern can be seen in August and December 2011, when the Hawke's Bay patch slips first, followed by the East Cape patch, and lastly the central Gisborne patch. The Gisborne event shows some migration in the updip direction. This 2011 Hawke's Bay, East Cape, and Gisborne sequence has smaller slip and slip-rate amplitudes compared to the similar 2010 sequence. In *Wallace et al.* [2012], evidence is presented for heterogenous frictional and pore fluid properties on the plate interface near Gisborne which may explain why the East Cape and Hawke's Bay patches tend to slip before the Gisborne patch in SSE sequences.

The offshore Cape Turnagain SSE in July 2011 begins on the southern end of its eventual extent and then spreads to the north over 30 days. After 9 days, slip ceases in the south, and a healing front propagates south to north following the migration of the slip front. Subsequent SSE episodes offshore from the east coast in 2011 are punctuated by periods of quiescence (lasting a few weeks to a month or more), with no clear north-south migration pattern during the sequence.

6. Seismic Swarm Associated With the 2011 Cape Turnagain SSE

During migration of the July 2011 Cape Turnagain SSE from south to north, a swarm of seismicity occurs concentrated in an area just to the west of the slipping region (Figure 10). This can be seen clearly in Animation S2, which shows the Cape Turnagain event's migration along with seismicity from the GeoNet catalog. Depths from the GeoNet earthquake catalog for these events range from 12 to 33 km, with most seismicity

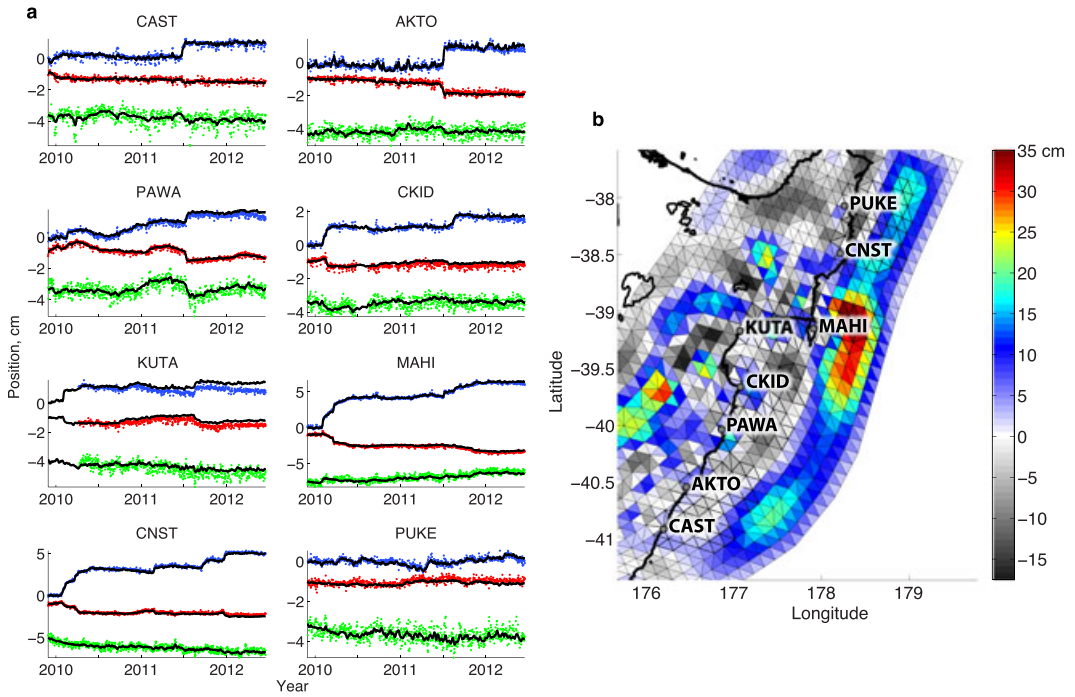

Figure 9. (a) Time-dependent fit to data for selected stations along the east coast of the North Island. Colored dots are data with outliers, seasonal signals, and inter-ETS velocities removed. Reference frame wobble as fit by the NIF is also removed. Black lines are model fits. Stations are ordered south to north. (b) Map of stations in Figure 9a, with final slip distribution.

in the range 25–30 km depth. This places the seismicity in the subducting slab, as the plate interface is about 15 km deep in this area. However, these locations are calculated using a New Zealand wide 1-D velocity model which is probably a poor representations for this offshore region.

Relocation with a 3-D velocity model (see section 3) places the seismicity significantly shallower, in the 10–20 km range. Double-difference relocation yields even shallower depths, placing the earthquakes within the upper place at depths shallower than 10 km. Errors in the locations due to velocity model uncertainty are estimated to be at least 10 km, and double-difference methods are known to reduce relative error between earthquakes but not necessarily absolute error in earthquake locations. The original GeoNet catalog and our relocations have very similar epicenters for the earthquakes; it is only the depth that changes significantly. We therefore conclude that it is impossible to determine with current data if this swarm is occurring above, on, or below the plate interface. For the remainder of this analysis, we use the official GeoNet earthquake locations.

The largest event in this seismic swarm is a M_w 4.8 event on 4 July 2011 (Figure 10a). The location and focal mechanism of this event in the GeoNet catalog are consistent with thrust on either the plate interface, or a

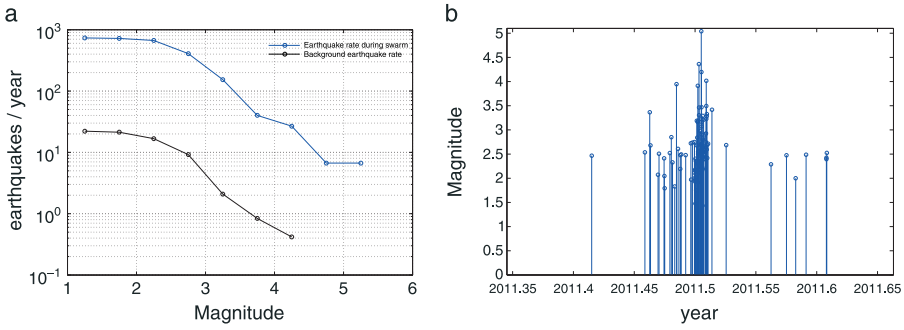

Figure 10. (a) Magnitude-rate plot for earthquakes within the bounding polygon shown in Figure 13 at any depth. Earthquake rates in this area increase by approximately a factor of 40 during the swarm. (b) Stem plot of magnitudes during the Cape Turnagain SSE swarm within the same bounding polygon.

higher angle splay fault in either the accretionary prism or the subducting slab as the mechanism is not well constrained (Table S1). Given this uncertainty, for the purposes of analyzing stress, we resolve shear stress on the plate interface in the direction of slip as specified by *Wallace et al.* [2004]. Although this may not be the correct slip location and direction for every event in the seismic swarm, it should provide a reasonable estimate of the relevant shear stress.

Intriguingly, the seismicity is confined to a relatively small area, and a relatively short time period, compared to the extent and duration of the Cape Turnagain SSE. This implies that there is something unique about this particular patch which makes it prone to SSE-associated seismicity. In a seismic profile through this area (*Barker et al.* [2009], profiles 05CM-38 and 05CM-41), the accretionary wedge above the seismically active patch is an area of high reflectivity, with many splay faults in the overriding plate. Without well-constrained depth estimates for this seismicity, it is impossible to determine whether these splay faults play a role in the confined spatial extent of the swarm.

6.1. Modeling Seismicity Rates Associated With the Cape Turnagain SSE

Assuming most of the seismicity during the Cape Turnagain SSE is on the plate interface, there are two possible triggering models. Either the earthquakes occur on locked asperities within the SSE region, stressed by the surrounding creep, or they occur outside the downdip extent of slow slip and are triggered by the stress increase outside the slipping region. Stress increases outside the slipping region can also explain triggered earthquakes above or below the plate interface. This distinction is important because it has implications for the largest possible triggered event. If the earthquakes are triggered on asperities within the slipping region, slip is confined to those asperities, and therefore, there is a maximum magnitude of triggerable event. If the earthquakes are triggered by stress outside the slow slip region, then it may be possible to trigger very large earthquakes during SSEs, bounded only by the size of the surrounding locked zone (Figure 1). The frequency-magnitude plot of this swarm appears to follow a Gutenberg-Richter law, with no indication of a maximum magnitude (Figure 10b).

The hypothesis of triggering outside of the slipping region is supported by the fact that the earthquakes occur near the downdip edge of the SSE, where the largest stress increases are expected, and not in the center of the slipping region as might be expected for earthquakes occurring on the locked patches within the slipping region. Additionally lithostatic pressure and thus fault normal stress are expected to increase with depth, with an accompanying transition between stable creep and stick-slip behavior. Consistent with this idea, *Wallace et al.* [2012] speculate that the Cape Turnagain SSE could occur in an updip velocity neutral zone along a transition from velocity weakening to velocity strengthening behavior on the megathrust, as opposed to a downdip transition from stick-slip to aseismic creep that SSEs are normally associated with.

We calculate a time-dependent shear stress on the plate interface using our time-dependent model of slip produced by the NIF. To do this, we assume a homogenous halfspace with shear modulus 30 GPa and calculate a stress tensor at the centroid of every triangle due to the combined effect of slip on all other triangles. We then resolve the shear and normal stresses on the interface in the assumed direction of slip. Shear stress on the plate interface calculated from the estimated slip distribution in the area of the earthquake swarm decreased during the Cape Turnagain SSE, making a static Coulomb stress triggering relationship seem unlikely at first glance (Figure 11). However, regularization employed in the NIF smoothes out the potentially sharp edge of the slip distribution, putting slip where there may not be any. If the true edge of slip is sharp, the largest stress increases will be in the area directly adjacent to the slipping region. Spatial smoothing in the NIF can make this area of highest shear stress increase appear to have decreased shear stress.

To model seismicity rate assuming a Coulomb stress triggering hypothesis, we use the method of *Segall et al.* [2006], based on the seismicity rate theory of *Dieterich* [1994]. This model assumes a stressing rate history broken into discrete intervals over which the stressing rate is assumed constant. The model does not include earthquakes triggered by previous earthquakes (aftershocks); however, there do not appear to be any obvious aftershock sequences within this swarm (Figure 10). We model the seismicity rate during the kth time interval given the stressing history in the swarm area up to the current time t. Seismicity rate as a function of time $R_k(t)$ is given as follows:

$$\frac{R_k(t)}{r} = \frac{1}{\dot{\tau}_r \gamma_k(t)} \tag{3}$$

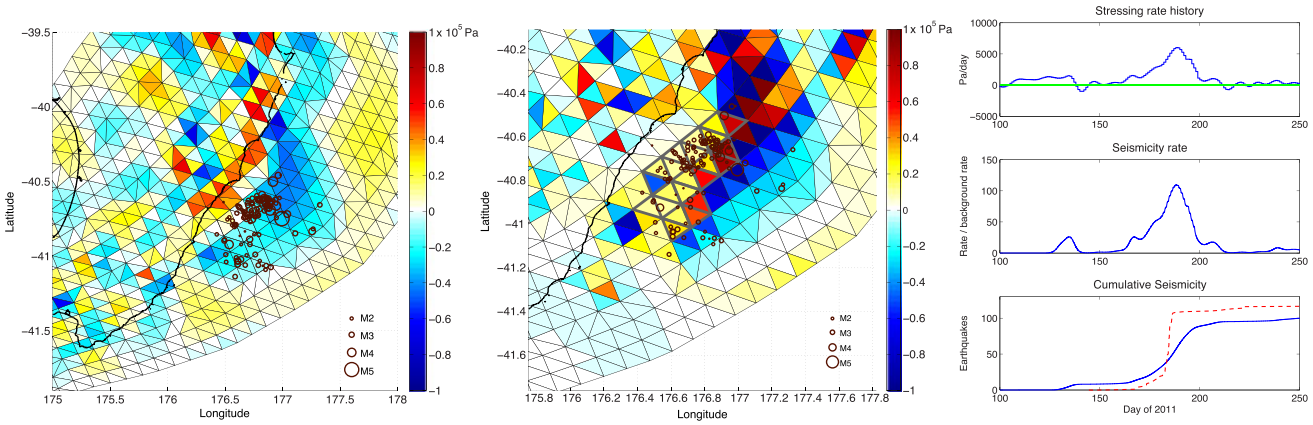

Figure 11. Total shear stress change on the plate interface from before the Cape Turnagain SSE until after from the NIF slip model. Locations of earthquakes during the event relocated using a 3-D velocity model are shown in brown.

where r is the background seismicity rate, $\dot{\tau}_r$ is the background stressing rate, and $\gamma_k(t)$ is a variable that evolves continuously in time according to

$$\gamma_k(t) = \left(\gamma_{k-1} - \frac{1}{\dot{\tau}_k}\right) \exp\left(\frac{-\dot{\tau}_r(t - t_{k-1})}{A\sigma}\right) + \frac{1}{\dot{\tau}_k} \tag{4}$$

where γ_{k-1} represents the value of γ at the end of the last time interval, $\dot{\tau}_k$ is the discrete interval stressing rate history, and $A\sigma$ is the product of a frictional parameter, A, and the effective normal stress, σ. The parameters needed to predict seismicity rate that are not obtained from the NIF are r, $\dot{\tau}_r$, and $A\sigma$. The background seismicity rate, r, is obtained from cumulative seismicity before the Cape Turnagain SSE and is found to be 0.0392 earthquakes/day. $\dot{\tau}_r$, and $A\sigma$ are related through the aftershock decay time t_a as

$$t_a = \frac{A\sigma}{\dot{\tau}_r}. \tag{5}$$

A nearby aftershock sequence a year before the Cape Turnagain SSE allows us to obtain t_a. We fit the seismicity rate after the main shock assuming a stress step and vary t_a (and therefore $A\sigma$) to fit the data. Although we do not know $\dot{\tau}_r$, we make an order of magnitude estimate based on plate convergence rate and plate locking of 0.02 MPa/yr. Because the seismicity rate is much more sensitive to t_a than to $\dot{\tau}_r$, this provides a sufficient estimate of $\dot{\tau}_r$. We find that t_a is approximately 25 days, which is similar to the 37 day value used by *Delahaye et al.* [2009] to model the swarm of seismicity associated with the 2004 Gisborne SSE.

To model the swarm associated with the Cape Turnagain swarm, we assume a boxcar function for stressing rate, i.e., a jump from background rate to a higher rate and a return to the background rate after a duration of 5 days. Although we do not know exactly the background stressing rate, we take our best estimate as before of 0.02 MPa/yr and pick the amplitude of the higher stressing rate during the swarm to fit the data. We find the best fit at an SSE-induced stressing rate of 6.0 MPa/yr, for a total stress change of about 82 kPa. The fit to the data for this model can be seen in Figure 12. This model gives a ratio of shear stressing rate to background ($\dot{\tau}/\dot{\tau}_r$) of 300, which is significantly larger than the value of 20 used by *Delahaye et al.* [2009] for the 2004 Gisborne SSE. However, this ratio is poorly constrained and dependant on the specific slip distribution during each SSE; so there is no reason to expect the same value in studies of two different SSE-associated swarms.

To further investigate the feasibility of the Coulomb triggering model, we perform a nonnegative least squares inversion of the GPS offsets in the Cape Turnagain region from before the Cape Turnagain SSE until after, with the constraint that stress in the swarm region go up by 82 kPa, as inferred from the change in seismicity rate (Figure 13). Laplacian spatial smoothing is implemented as in the NIF. This model fits the data adequately, showing that it is possible to fit the data and increase the stress enough to explain the seismic swarm with a Coulomb triggering hypothesis. This does not, however, preclude a model in which the earthquakes occur on locked asperities within the slow slip region. To test that hypothesis, it would be useful to

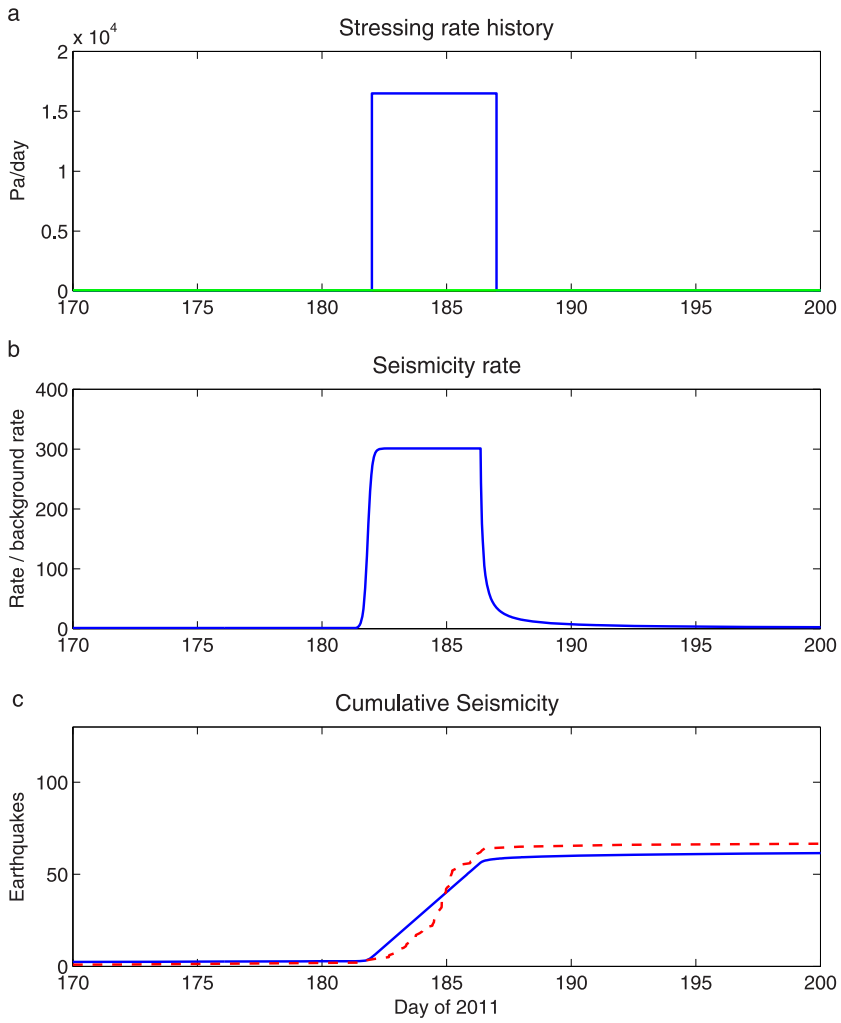

Figure 12. (a) Best fitting stressing rate boxcar model (blue line) with a background stressing rate of 20 kPa/yr and stressing rate during the swarm of 6 MPa/yr ≈ 16 kPa/d. Green line represents the background stressing rate. (b) Predicted seismicity rate relative to background and (c) predicted cumulative seismicity (blue line) and actual cumulative seismicity (red dashed line).

look for repeating characteristic earthquakes that indicate repeated slip on the same patch. Or, if the earthquakes could be shown to be not on the plate interface, it would prove that they were therefore not within the slipping region. However, this is outside the scope of this work.

7. Tremor and Slow Slip Events in Hikurangi

The strongest evidence for tectonic tremor in the Hikurangi subduction zone comes from the studies of *Ide* [2012], *Fry et al.* [2011], and *Kim et al.* [2011]. These studies find tremor near the Manawatu and Gisborne regions. There may also be tremor in other regions that remains to be discovered. In the Gisborne region the offshore locations and highly attenuating nature of the area make these tremor catalogs sparse. The catalog of tremor in the Manawatu region reported by *Ide* [2012] is more complete but does not cover the time of strong SSE slip in the Manawatu region, making investigation of a temporal correlation between slip and tremor difficult at this time. The depths of tremor sources are poorly resolved, and it is not clear if tremor is on the plate interface.

Spatially, tremor locations reported by *Ide* [2012] locate on a roughly linear feature near the 60 km plate interface contour near the downdip edge of the Manawatu slow slip patch (Figure 14). This is in contrast to colocated tremor and slip in Nankai and Cascadia [e.g., *Hirose and Obara*, 2010; *Bartlow et al.*, 2011], but is

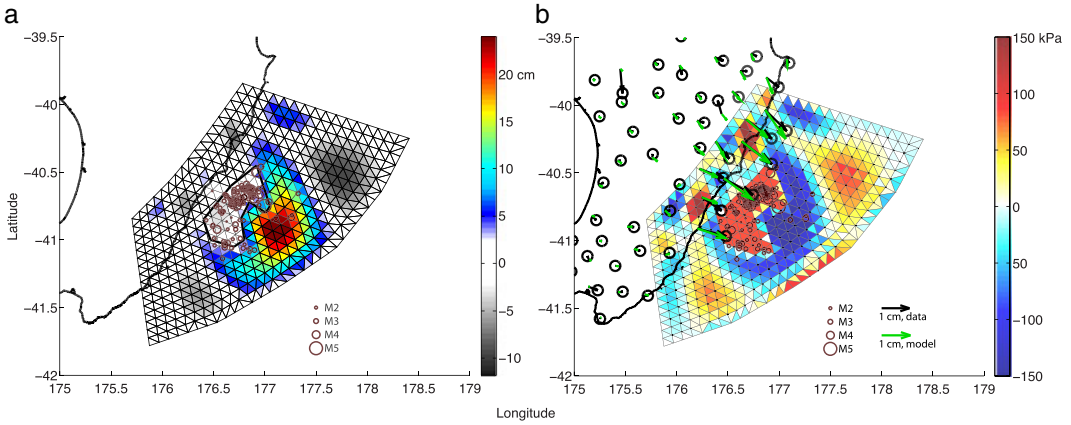

Figure 13. (a) Slip distribution for the Cape Turnagain SSE resulting from a constrained regularized time independent GPS inversion. Black polygon is the bounding polygon referred to in Figure 10. (b) Shear stress change corresponding to the slip distribution in Figure 13a. Shear stress was constrained to increase by 82 kPa in the region of the Cape Turnagain SSE swarm, which is enough to explain the cumulative seismicity observed (see Figure 12). Black vectors and error ellipses show GPS offsets, and green vectors show model fits.

similar to observations of tremor downdip of slow slip in the Bungo Channel area of Japan, and the Guerrero gap in Mexico (see section 8). At this time, the relationship between the slow slip and tremor is unclear, but a Coulomb triggering relationship similar to the discussion in section 6.1 is possible.

Tremor triggered by the 2010 Maule earthquake has been observed in the same location as the ambient tremor detected by *Ide* [2012] and *Fry et al.* [2011]. In *Fry et al.* [2011], the tremor locations were constrained to the plate interface. *Fry et al.* [2011] speculates that this area is prone to tremor because of low friction and increased fluid pressure on the plate interface. They further speculate that this state is caused by a mass of fluid-rich underplated sediment that dehydrates at this depth.

8. Comparison of Hikurangi SSEs to Other Regions

SSEs at the Hikurangi margin show unique features not observed in the better studied Cascadia and Nankai examples of episodic tremor and slip (ETS). Unlike Cascadia and Nankai, New Zealand SSEs are not accompanied by abundant tremor, although some are associated with microseismicity. At Hikurangi there

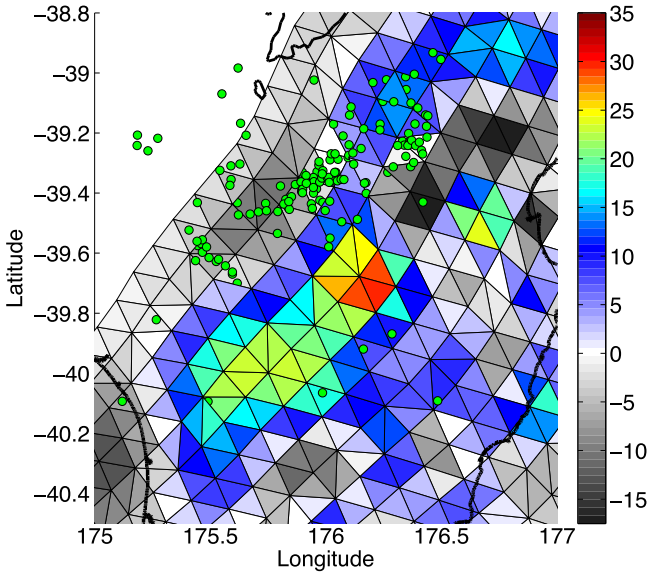

Figure 14. Tremor epicenters (green dots) in the region of the Manawatu SSE for the period 2 September 2004 to 29 June 2010, from *Ide* [2012]. Color represents slip during the Manawatu SSE (dates defined in Table 1).

are shallow SSEs lasting less than 4 weeks as well as deep SSEs lasting almost 1 year. The shallow Cape Turnagain SSE slip is updip of the deep Manawatu SSE, with background seismicity in between, implying a substantial downdip variation in slip behavior. In Cascadia, all SSEs occur at essentially the same depth and have durations less than 4 weeks [e.g., *Schmidt and Gao*, 2010]. Cascadia SSEs recur on a rather predictable basis, for example, every 12–14 months in the Puget Sound area [*Brudzinski and Allen*, 2007], in contrast to New Zealand SSEs which have more irregular recurrence patterns [*Wallace and Beavan*, 2010]. In southwest Japan, both long-term (Bungo Channel) and short-term (Shikoku/southwest Honshu ETS) SSEs are observed, with the long-term SSEs updip of the short-term ETS, not downdip as in Hikurangi [*Hirose and Obara*, 2005; *Hirose et al.*, 2010]. This shows that there is not a simple worldwide correlation between depth and duration of SSEs. The largest Hikurangi SSEs also have a lot more slip (20+ cm, see Table 1) than Cascadia or Nankai ETS events, which generally have less than 6 cm of slip. Peak slip rates in Cascadia and Nankai ETS are approximately 0.4 cm/d and 0.8 cm/d, respectively, similar to the range of peak slip rates in Hikurangi SSEs (Table 1) [e.g., *Dragert et al.*, 2001; *Hirose and Obara*, 2005; *Ozawa et al.*, 2007a; *Hirose and Obara*, 2010; *Bartlow et al.*, 2011].

The shallow, east coast SSEs are similar to shallow SSEs in the Boso Peninsula, central Japan. Both sets of SSEs have similar depths, durations, equivalent moment magnitudes, and strong relationship with microseismicity. Boso SSEs occur less frequently than Hikurangi SSEs, and involve relatively high peak slip rates (1–1.4 cm/d; estimated from *Ozawa et al.* [2007a]), in line with the most rapidly slipping SSEs in New Zealand, such as the large Gisborne 2010 SSE (peak slip 1.1 cm/d). The clear temporal correlation between microseismicity swarms and Boso Peninsula SSEs is similar to microseismicity accompanying the 2010 Gisborne and 2011 Cape Turnagain SSEs. Additionally, in all three of these cases, the seismicity is located downdip of the slipping region. At least for the 2010 Gisborne SSE and Boso SSEs, the peak slip rates are higher than for most other SSEs (1 cm/d or more, compared to less than 0.5 cm/d), implying higher shear stressing rates in the adjacent region, consistent with the stress triggering model presented in section 6.1 (although this does not exclude other triggering models). However, we note that the 2011 Cape Turnagain SSE had a peak slip rate of only 0.5 cm/d. It is possible that the shear stressing rate in the region adjacent to the Cape Turnagain event was high despite a relatively low slip rate because of a steep gradient in slip near the edge of the slipping region. Additionally, the shallow depth of the Cape Turnagain SSE implies low relatively normal stress, which lowers the threshold for triggering (equations (3) and (4)).

The Manawatu event, and its spatial relationship to tremor (Figure 14) bears similarities to slow slip and tremor in Guerrero, Mexico, and in the Bungo Channel of southwest Japan. In all three of these examples, SSEs are large ($M_w \approx 7.0$ equivalent), long (7–20 months), and deep (30–50 km depth). Similar to Manawatu, tremor has been observed along the downdip limit of slow slip in Mexico [*Brudzinski et al.*, 2010; *Kostoglodov et al.*, 2010] and Bungo Channel [*Hirose and Obara*; 2005; *Ozawa et al.*, 2007b], but generally not within the slowly slipping area. Guerrero SSEs accumulate about 10 cm of slip, while Bungo Channel SSEs have 30-40 cm of slip and peak slip rates of approximately 0.1 cm/d (estimated from *Kostoglodov et al.* [2010] and *Ozawa et al.* [2007b]). These values are similar to those for the Manawatu SEE (Table 1). Additionally, the Bungo channel SSEs also show a multiphase progression with slip rate vanishing between phases, similar to our observations of the Manawatu SSE [*Ozawa et al.*, 2007b].

While all depths, durations, magnitudes, and slip amplitudes included here are subject to uncertainty, our comparisons rely on differences that are at least a factor of 2 in these parameters, which should be larger than any uncertainties.

9. Conclusions

In this study we observe a large variation in slow slip behavior in the Hikurangi margin during 2010 and 2011. Durations, depths, total slip, and slip rates all vary by almost an order of magnitude within this subduction zone. Hikurangi slow slip is not as regular or predictable as in other well-studied regions. Repeated SSEs in the same region, for example, Gisborne or the East Cape, have very different magnitudes and amounts of slip. This makes Hikurangi markedly different from the well-studied areas of southwest Japan and Cascadia, and a good place for further study of a wide range of slow slip behavior.

We further analyze the seismic swarm associated with the Cape Turnagain SSE but are unable to determine the mechanism of triggering between the SSE and the swarm; however, triggering by static stress

increase outside the slipping region seems plausible. We also compare the tremor locations of *Ide* [2012] to our model of the Manawatu SSE and show that tremor and slow slip in Hikurangi are not colocated as they are for short-term SSEs in Japan and Cascadia. However, the Manawatu SSE appears similar to the Bungo Channel SSE, with tremor on the downdip edge and similar durations and amounts of slip.

The 2010–2011 SSE sequence demonstrates the wide range of SSE behavior observed in the Hikurangi margin. Outside of our time period of study, SSEs have been observed in additional locations in Hikurangi as well [*Wallace and Beavan*, 2010]. Additionally, the permanent network of seismic and geodetic instruments maintained by GeoNet continue to make Hikurangi an excellent place to study SSEs.

Acknowledgments

The authors would like to thank Andrew M. Bradley and Yo Fukushima for contributing MATLAB code used in this work, and Satoshi Ide, Aaron Wech, and Suguru Yabe for helpful discussions. We also thank John Townend and one anonymous reviewer for their helpful comments. Noel Bartlow's role in this work was funded by an NSF Graduate Research Fellowship, a Stanford Gabilan Graduate Fellowship, and an NSF East Asia and Pacific Summer Institutes (EAPSI) Fellowship. A large portion of this work was performed while Noel Bartlow was working with John Beavan as a visitor at GNS Science from June to August 2012, prior to his death in November 2012.

References

Aguiar, A. C., T. I. Melbourne, and C. W. Scrivner (2009), Moment release rate of Cascadia tremor constrained by GPS, *J. Geophys. Res.*, *114*, B00A05, doi:10.1029/2008JB005909.

Ansell, J., and S. Bannister (1996), Shallow morphology of the subducted Pacific Plate along the Hikurangi margin, New Zealand, *Phys. Earth Planet Inter.*, *93*, 3–20.

Audet, P., M. G. Bostock, N. I. Christensen, and S. M. Peacock (2009), Seismic evidence for overpressured subducted oceanic crust and megathrust fault sealing, *Nature*, *457*(7225), 76–78, doi:10.1038/nature07650.

Baltay, A., S. Ide, G. Prieto, and G. Beroza (2011), Variability in earthquake stress drop and apparent stress, *Geophys. Res. Lett.*, *38*, L06303, doi:10.1029/2011GL046698.

Barker, D. H. N., R. Sutherland, S. Henrys, and S. Bannister (2009), Geometry of the Hikurangi subduction thrust and upper plate, North Island, New Zealand, *Geochem. Geophys. Geosyst.*, *10*, Q02007, doi:10.1029/2008GC002153.

Bartlow, N. M., S. Miyazaki, A. M. Bradley, and P. Segall (2011), Space-time correlation of slip and tremor during the 2009 Cascadia slow slip event, *Geophys. Res. Lett.*, *38*, L18309, doi:10.1029/2011GL048714.

Bartlow, N. M., D. A. Lockner, and N. M. Beeler (2012), Laboratory triggering of stick-slip events by oscillatory loading in the presence of pore fluid with implications for physics of tectonic tremor, *J. Geophys. Res.*, *117*, B11411, doi:10.1029/2012JB009452.

Beavan, R. J. (2005), Noise properties of continuous GPS data from concrete pillar geodetic monuments in New Zealand, and comparison with data from U.S. deep drilled braced monuments, *J. Geophys. Res.*, *110*, B08410, doi:10.1029/2005JB003642.

Bell, R., R. Sutherland, D. H. N. Barker, S. Henrys, S. Bannister, L. Wallace, and J. Beavan (2010), Seismic reflection character of the Hikurangi subduction interface, New Zealand, in the region of repeated Gisborne slow slip events, *Geophys. J. Int.*, *180*(1), 34–48, doi:10.1111/j.1365-246X.2009.04401.x.

Brown, J. R., G. C. Beroza, S. Ide, K. Ohta, D. R. Shelly, S. Y. Schwartz, W. Rabbel, M. Thorwart, and H. Kao (2009), Deep low-frequency earthquakes in tremor localize to the plate interface in multiple subduction zones, *Geophys. Res. Lett.*, *36*, L19306, doi:10.1029/2009GL040027.

Brudzinski, M. R., and R. M. Allen (2007), Segmentation in episodic tremor and slip all along Cascadia, *Geology*, *35*, 907–910, doi:10.1130/G23740A.1.

Brudzinski, M. R., H. R. Hinojosa-Prieto, K. M. Schlanser, E. Cabral-Cano, A. Arciniega-Ceballos, O. Diaz-Molina, and C. DeMets (2010), Nonvolcanic tremor along the Oaxaca segment of the Middle America subduction zone, *J. Geophys. Res.*, *115*, B00A23, doi:10.1029/2008JB006061.

Dach, R., U. Hugentobler, P. Fridez, and M. Meindl (2007), *Bernese GPS Software Version 5.0*, 612 pp., Astron. Inst., Univ. of Bern, Bern, Switzerland.

Delahaye, E. J., J. Townend, M. Reyners, and G. Rodgers (2009), Microseismicity but no tremor accompanying slow slip in the Hikurangi subduction zone, New Zealand, *Earth Planet. Sci. Letters*, *277*, 21–28, doi:10.1016/j.epsl.2008.09.038.

Dieterich, J. (1994), A constitutive law for rate of earthquake production and its application to earthquake clustering, *J. Geophys. Res.*, *99*(B2), 2601–2618, doi:10.1029/93JB02581.

Douglas, A., J. Beavan, L. Wallace, and J. Townend (2005), Slow slip on the northern Hikurangi subduction interface, New Zealand, *Geophys. Res. Lett.*, *32*, L16305, doi:10.1029/2005GL023607.

Dragert, H., K. Wang, and T. James (2001), A silent slip event on the deeper Cascadia subduction interface, *Science*, *292*, 1525–1528, doi:10.1126/science.1060152.

Eberhart-Phillips, D., M. Reyners, M. Chadwick, and J.-M. Chiu (2005), Crustal heterogeneity and subduction processes: 3-D Vp, Vp/Vs and Q in the southern North Island, New Zealand, *Geophys. J. Int.*, *162*, 270–288, doi:10.1111/j.1365-246X.2005.02530.x.

Eberhart-Phillips, D., M. Reyners, S. Bannister, M. Chadwick, and S. Ellis (2010), Establishing a versatile 3-D seismic velocity model for New Zealand, *Seismol. Res. Lett.*, *81*, 992–1000, doi:10.1785/?gssrl.81.6.992.

Fagereng, A., and S. Ellis (2009), On factors controlling the depth of intersesimic coupling on the Hikurangi subduction interface, New Zealand, *Earth Planet. Sci. Letters*, *278*, 120–130, doi:10.1016/j.epsl.2008.11.033.

Fukuda, J., T. Higuchi, S. Miyazaki, and T. Kato (2004), A new approach to time-dependent inversion of geodetic data using a Monte Carlo mixture Kalman filter, *Geophys. J. Int.*, *159*(1), 17–39, doi:10.1111/j.1365-246X.2004.02383.x.

Fry, B., K. Chao, S. Bannister, Z. Peng, and L. Wallace (2011), Deep tremor in New Zealand triggered by the 2010 M_w 8.8 Chile earthquake, *Geophys. Res. Lett.*, *38*, L15306, doi:10.1029/2011GL048319.

Hirose, H., and K. Obara (2005), Repeating short- and long-term slow slip events with deep tremor activity around the Bungo channel region, southwest Japan, *Earth Planets Space*, *57*, 961–972.

Hirose, H., and K. Obara (2010), Recurrence behavior of short-term slow slip and correlated nonvolcanic tremor episodes in western Shikoku, southwest Japan, *J. Geophys. Res.*, *115*, B00A21, doi:10.1029/2008JB006050.

Hirose, H., Y. Asano, K. Obara, T. Kimura, T. Matsuzawa, S. Tanaka, and T. Maeda (2010), Slow earthquakes linked along dip in the Nankai subduction zone, *Science*, *330*, 1502, doi:10.1126/science.1197102.

Ide, S., D. R. Shelly, and G. C. Beroza (2007), Mechanism of deep low frequency earthquakes: Further evidence that deep non-volcanic tremor is generated by shear slip on the plate interface, *Geophys. Res. Lett.*, *34*, L03308, doi:10.1029/2006GL028890.

Ide, S. (2012), Variety and spatial heterogeneity of tectonic tremor worldwide, *J. Geophys. Res.*, *117*, B03302, doi:10.1029/2011JB008840.

Ito, Y., et al. (2013), Episodic slow slip events in the Japan subduction zone before the 2011 Tohoku-Oki earthquake, *Tectonophysics*, *600*, 14–26, doi:10.1016/j.tecto.2012.08.022.

Kato, A., K. Obara, T. Igarashi, H. Tsuruoka, S. Nakagawa, and N. Hirata (2011), Propagation of slow slip leading Up to the M_w 9.0 Tohoku-Oki earthquake, *Science*, *335*(6069), 705–708, doi:10.1126/science.1215141.

Kim, M. Y., S. Y. Schwartz, and S. Bannister (2011), Non-volcanic tremor associated with the March 2010 Gisborne slow slip event at the Hikurangi subduction margin, New Zealand, *Geophys. Res. Lett.*, *38*, L14301, doi:10.1029/2011GL048400.

Kitajima, H., and D. M. Saffer (2012), Elevated pore pressure and anomalously low stress in regions of low frequency earthquakes along the Nankai Trough subduction megathrust, *Geophys. Res. Lett.*, *39*, L23301, doi:10.1029/2012GL053793.

Kodaira, S., T. Iidata, A. Kato, J.-O. Park, T. Iwasaki, and Y. Kaneda (2004), High pore fluid pressure may cause silent slip in the Nankai trough, *Science*, *304*(5675), 1295–1298, doi:10.1126/science.1096535.

Kostoglodov, V., A. Husker, N. M. Shapiro, J. S. Payero, M. Campillo, N. Cotte, and R. Clayton (2010), The 2006 slow slip event and nonvolcanic tremor in the Mexican subduction zone, *Geophys. Res. Lett.*, *37*, L24301, doi:10.1029/2010GL045424.

Larson, K. M., V. Kostoglodov, A. Lowry, W. Hutton, O. Sanchez, K. Hudnut, and G. Suarez (2004), Crustal deformation measurements in Guerrero, Mexico, *J. Geophys. Res.*, *109*, B04409, doi:10.1029/2003JB002843.

Liu, Y., and J. R. Rice (2005), Aseismic slip transients emerge spontaneously in three dimensional rate and state modeling of subduction earthquake sequences, *J. Geophys. Res.*, *110*, B08307, doi:10.1029/2004JB003424.

Liu, Y., and J. R. Rice (2007), Spontaneous and triggered aseismic deformation transients in a subduction fault model, *J. Geophys. Res.*, *112*, B09404, doi:10.1029/2007JB004930.

Mazzotti, S., and J. Adams (2004), Variability of Near-Term Probability for the Next Great Earthquake on the Cascadia Subduction Zone, *Bull. Seismol. Soc. Am.*, *94*(4), 1954–1959, doi:10.1785/012004032.

McGuire, J. J., and P. Segall (2003), Imaging of aseismic fault slip transients recorded by dense geodetic networks, *Geophys. J. Int.*, *155*(3), 778–788, doi:10.1111/j.1365-246X.2003.02022.x.

Miyazaki, S., P. Segall, J. J. McGuire, T. Kato, and Y. Hatanaka (2006), Spatial and temporal evolution of stress and slip rate during the 2000 Tokai slow earthquake, *J. Geophys. Res.*, *111*, B03409, doi:10.1029/2004JB003426.

Mortimer, N., and D. Parkinson (1996), Hikurangi Plateau: A Cretaceous large igneous province in the southwest Pacific Ocean, *J. Geophys. Res.*, *101*(B1), 687–696, doi:10.1029/95JB03037.

Ohta, Y., F. Kimata, and T. Sagiya (2004), Reexamination of the interplate coupling in the Tokai region, central Japan, based on the GPS data in 1997–2002, *Geophys. Res. Lett.*, *31*, L24604, doi:10.1029/2004GL021404.

Ohta, Y., J. T. Freymueller, S. Hreinsdottir, and H. Suito (2006), A large slow slip event and the depth of the seismogenic zone in the south central Alaska subduction zone, *Earth Planet. Sci. Lett.*, *247*, 108–116, doi:10.1016/j.epsl.2006.05.013.

Ozawa, S., H. Suito, and M. Tobita (2007a), Occurrence of quasi-periodic slow slip off the east coast of the Boso Peninsula, Central Japan, *Earth Planets Space*, *59*, 1241–1245.

Ozawa, S, H. Suito, T. Imakiire, and M. Murakmi (2007b), Spatiotemporal evolution of aseismic interplate slip between 1996 and 1998 and between 2002 and 2004, in Bungo Channel, southwest Japan, *J. Geophys. Res.*, *112*, B05409, doi:10.1029/2006JB004643.

Reyners, M., and D. Eberhart-Phillips (2009), Small earthquakes provide insight into plate coupling and fluid distribution in the Hikurangi subduction zone, New Zealand, *Earth Planet. Sci. Lett.*, *282*(1–4), 299–305, doi:10.1016/j.epsl.2009.03.034.

Reyners, M., D. Eberhart-Phillips, G. Stuart, and Y. Nishimura (2006), Imaging subduction from the trench to 300 km depth beneath the central North island, New Zealand, with Vp and Vp/Vs, *Geophys. J. Int.*, *165*, 565–583, doi:10.1111/j.1365-246X.2006.02897.x.

Sagiya, T. (2004), Interplate coupling in the Kanto District, central Japan, and the Boso Peninsula Silent Earthquake in May 1996, *Pure Appl. Geophys.*, *161*, 2327–2342, doi:10.1007/s00024-004-2566-6.

Schmidt, D. A., and H. Gao (2010), Source parameters and time-dependent slip distributions of slow slip events on the Cascadia subduction zone from 1998 to 2008, *J. Geophys. Res.*, *115*, B00A18, doi:10.1029/2008JB006045.

Segall, P., and A. M. Bradley (2012), Slow-slip evolves into megathrust earthquakes in 2D numerical simulations, *Geophys. Res. Lett.*, *39*, L18308, doi:10.1029/2012GL052811.

Segall, P., E. K. Desmarais, D. Shelly, A. Miklius, and P. Cervelli (2006), Earthquakes triggered by silent slip events on Kilauea volcano, *Nature*, *442*, 71–74, doi:10.1038/nature04938.

Segall, P., and M. Matthews (1997), Time dependent inversion of geodetic data, *J. Geophys. Res.*, *102*, 22,391–22,409.

Shaw, B. E. (2009), Constant stress drop from small to great earthquakes in magnitude-area scaling, *Bull. Seismol. Soc. Am.*, *99*, 871–875, doi:10.1785/0120080006.

Shelly, D. R., G. C. Beroza, S. Ide, and S. Nakamula (2006), Low-frequency earthquakes in Shikoku, Japan, and their relationship to episodic tremor and slip, *Nature*, *442*(7099), 188–191, doi:10.1038/nature04931.

Shelly, D. R., G. C. Beroza, and S. Ide (2007), Non-volcanic tremor and low-frequency earthquake swarms, *Nature*, *446*(7133), 305–307, doi:10.1038/nature05666.

Song, T. A., D. V. Helmberger, M. R. Brudzinski, R. W. Clayton, P. Davis, X. Perez-Campos, and S. K. Singh (2009), Subducting slab ultra-slow velocity layer coincident with silent earthquakes in southern Mexico, *Science*, *324*, 502–506, doi:10.1126/science.1167595.

Townend, J., S. Sherburn, R. Arnold, C. Boese, and L. Woods (2012), Three-dimensional variations in present-day tectonic stress along the Australia Pacific plate boundary in New Zealand, *Earth Planet. Sci. Letters*, *353–354*, 47–59, doi:10.1016/j.epsl.2012.08.003.

Thomas, A. L. (1993), Poly3D: A three-dimensional, polygonal element, displacement discontinuity boundary element computer program with applications to fractures, faults, and cavities in the Earth's crust, M.S. thesis, Dep. of Geol. and Environ. Sci., Stanford Univ., Stanford, Calif.

Waldhauser, F., and W. L. Ellsworth (2000), A double-difference earthquake location algorithm: Method and application to the northern Hayward fault, California, *Bull. Seismol. Soc. Am.*, *90*, 1353–1368, doi:10.1785/0120000006.

Wallace, L. M., and J. Beavan (2006), A large slow slip event on the central Hikurangi subduction interface beneath the Manawatu region, North Island, New Zealand, *Geophys. Res. Lett.*, *33*, L11301, doi:10.1029/2006GL026009.

Wallace, L. M., and J. Beavan (2010), Diverse slow slip behavior at the Hikurangi subduction margin, New Zealand, *J. Geophys. Res.*, *115*, B12402, doi:10.1029/2010JB007717.

Wallace, L. M., R. J. Beavan, R. McCaffrey, and D. J. Darby (2004), Subduction zone coupling and tectonic block rotations in the North Island, New Zealand, *J. Geophys. Res.*, *109*, B12406, doi:10.1029/2004JB003241.

Wallace, L. M., et al. (2009), Characterizing the seismogenic zone of a major plate boundary subduction thrust: Hikurangi Margin, New Zealand, *Geochem. Geophys. Geosyst.*, *10*, Q10006, doi:10.1029/2009GC002610.

Wallace, L. M., J. Beavan, Bannister, and C. Williams (2012), Simultaneous long-term and short-term slow slip events at the Hikurangi subduction margin, New Zealand: Implications for processes that control slow slip event occurrence, duration, and migration, *J. Geophys. Res.*, *117*, B11402, doi:10.1029/2012JB009489.

Wallace, L. M., and D. Eberhart-Phillips (2013), Newly observed, deep slow slip events at the central Hikurangi margin, New Zealand: Implications for downdip variability of slow slip and tremor, and relationship to seismic structure, *Geophys. Res. Lett.*, *40*, 5393–5398, doi:10.1002/2013GL057682.

Wang, K., and S. L. Bilek (2011), Do subducting seamounts generate or stop large earthquakes?, *Geology*, *39*, 819–822, doi:10.1130/G31856.1.

Wdowinski, S., Y. Bock, J. Zhang, P. Fang, and J. Genrich (1997), Southern California Permanent GPS Geodetic Array: Spatial filtering of daily positions for estimating coseismic and postseismic displacements induced by the 1992 Landers earthquake, *J. Geophys. Res.*, *102*, 18,057–18,070, doi:10.1029/97JB01378.

Zhang, H. J., and C. H. Thurber (2003), Double-difference tomography: The method and its application to the Hayward Fault, California, *Bull. Seismol. Soc. Am.*, *93*, 1875–1889, doi:10.1785/0120020190.